metals

MDPI

Article

Effect of Mo on Corrosion Performance of Inner Bottom Plate of Corrosion-Resistant Storage Tank Steel

Jun Hong [1,2], Yuanyuan Chen [1], Yongqi Yang [1], Ruize Zhang [1], Chuyan Zhou [3], Qiang Yu [3] and Qingfeng Wang [1,*]

[1] State Key Laboratory of Metastable Materials Science & Technology, Yanshan University, Qinhuangdao 066004, China
[2] Nanjing Iron & Steel United Co., Ltd., Nanjing 210035, China
[3] Hebei Technology Innovation Center for Multimodal Intelligent Detection in Discrete Manufacturing, Cangzhou Normal University, Cangzhou 061001, China
* Correspondence: wqf67@ysu.edu.cn; Tel.: +86-335-2039067

Abstract

To explore the improvement of the corrosion resistance of the inner bottom plate of corrosion-resistant storage tank steel and the effects and underlying mechanisms of varying molybdenum (Mo) contents (0Mo, 0.15 wt.%Mo, 0.30 wt.%Mo, and 0.60 wt.%Mo), a systematic study is conducted on the corrosion performance of the steel in a simulated environment (10 wt.% NaCl solution, 30 ± 1 °C). The findings reveal that the steel containing 0.3 wt.% Mo possesses superior corrosion resistance. An optimal dosage of Mo refines corrosion products and fills voids via the formation of nano-scale MoO_2/MoO_3 particles, mediates the evolution of γ-FeOOH towards α-FeOOH, and improves the protective capability and electrochemical stability of the rust layer. Nevertheless, excessive Mo leads to the residual of elemental Mo arising from incomplete oxidation, which constructs a galvanic cell with Fe, thereby accelerating corrosion. Additionally, an excessively high proportion of MoO_3 triggers elevated internal stress and structural degradation of the rust layer.

Keywords: storage tank steel; corrosion resistance; Mo; electrochemical stability

1. Introduction

The development of energy strategic reserves and the chemical industry has led to the extensive deployment of large-scale corrosion-resistant storage tanks in fields including petroleum, chemical engineering, and LNG. These tanks are subjected to harsh service environments involving corrosive media (e.g., sulfur-containing and chlorine-containing substances), as well as low temperatures and high pressures. The tanks demand that the applied steel fulfills the demanding criteria of excellent corrosion resistance, high strength, high toughness, and good weldability, all essential for structural integrity and prolonged service life [1,2]. The synergistic effects of Cl^- attack, electrochemical corrosion, and rust layer spallation tend to induce corrosion failure of the steel, which not only shortens the service life of storage tanks, but also may trigger safety hazards such as medium leakage [3,4]. Therefore, the development of storage tank steel with long-term corrosion resistance, structural stability, and economic efficiency has become a core demand in the fields of marine engineering and chemical storage, and the precise regulation of alloying elements is a crucial approach to optimizing the corrosion resistance of steel.

Most current storage tank steels achieve a protective rust layer primarily via the incorporation of alloying elements, including Ni, Cr, and Cu, yet they suffer from notable limitations. Although high-Ni steels can form the stable $NiFe_2O_4$ phase beneficial for rust

Check for updates

Academic Editor: Eric Hug

Received: 15 January 2026
Revised: 3 February 2026
Accepted: 9 February 2026
Published: 14 February 2026

Copyright: © 2026 by the authors. Licensee MDPI, Basel, Switzerland. This article is an open access article distributed under the terms and conditions of the Creative Commons Attribution (CC BY) license.

layer protectiveness, the high cost of Ni compromises its economic feasibility for large-scale use. Concurrently, establishing a fully protective rust layer in high-salt conditions presents considerable difficulty [5,6]. For Cr-containing steels, while Cr enrichment enables the formation of Cr_2O_3 to improve rust layer stability, Cr^{3+} is prone to hydrolysis, leading to an elevated risk of rust layer failure [7,8]. Furthermore, the regulation of a single alloying element is insufficient to address the complexity of multi-factor synergistic corrosion in storage tank environments, highlighting an urgent need to develop novel microalloying strategies to overcome existing bottlenecks [9].

Molybdenum (Mo), a typical corrosion-resistant microalloying element, exhibits unique advantages in inhibiting Cl^- penetration and optimizing rust layer structure, offering a novel avenue for the performance upgrading of storage tank steel [10,11]. Existing studies have confirmed that Mo can be oxidized to form nano-sized MoO_2 and MoO_3 particles during corrosion, which not only fill pores in the rust layer and refine corrosion products, but also stabilize key protective phases such as $NiFe_2O_4$, inhibiting their dissolution and degradation to maintain the electronegativity of the rust layer for impeding Cl^- invasion [12,13]. Mo catalyzes the transformation of metastable rust phases (γ-FeOOH, β-FeOOH) into the stable α-FeOOH, thereby improving the compactness and protective durability of the layer [14,15]. Furthermore, Mo acts synergistically with Ni and Cr to amplify the rust layer's physical barrier and chemical passivation effects. Its dose-dependent influence thereby provides a viable pathway for optimizing the alloy composition [15,16].

However, numerous unresolved issues regarding the application of Mo in storage tank steel still urgently require clarification. Firstly, the mechanism of Mo action in the specific corrosion environment of storage tanks has not been systematically elucidated, and targeted investigations into the regulatory laws governing its effects on rust layer structure, phase composition, and electrochemical behavior are lacking. Additionally, existing studies have revealed that excessive Mo addition exerts a detrimental effect on corrosion resistance, yet the underlying mechanism of this deterioration remains to be thoroughly analyzed. Finally, the regulatory role of Mo in rust layer evolution during the long-term service of storage tank steel has not been clearly defined, making it difficult to provide reliable support for compositional design in engineering applications.

Based on the aforementioned research gaps, this study focuses on simulating the typical corrosive environments of storage tanks to systematically investigate the regulatory effects and underlying mechanisms of Mo on the corrosion resistance of storage tank steel. By employing corrosion kinetics tests, microstructural morphology characterization, phase composition analysis, and electrochemical measurements, the study clarifies the regulatory rules of Mo on the densification of rust layer structure, optimization of phase composition, and enhancement of electrochemical stability, while elucidating its corrosion resistance mechanism. The findings of this work provide a crucial theoretical basis and technical support for the compositional optimization design of storage tank steel and hold significant engineering value for improving the service life and safety reliability of storage tank equipment in harsh corrosive environments.

2. Experiments

2.1. Test Materials and Preparation

Experimental steels with different molybdenum (Mo) contents were smelted in an 80 kg small-scale vacuum furnace, with one heat conducted for each steel grade, and then cast into single ingots. Samples were taken from the central part of the steel ingots, and the chemical compositions of the experimental steels were determined by a direct-reading spectrometer and chemical analysis method, with the results shown in Table 1. These

are referred to as 0Mo, 15Mo, 30Mo, and 60Mo steels. After verifying that the chemical composition test results met the specified requirements, the finished experimental steel plates with a thickness of 18 mm were produced on a pilot rolling mill by means of the two-stage rolling and controlled cooling process, namely the Thermo-Mechanical Control Process (TMCP). The schematic diagram of the specific process is illustrated in Figure 1. The metallographic structure of the specimens can be found in detail in [1].

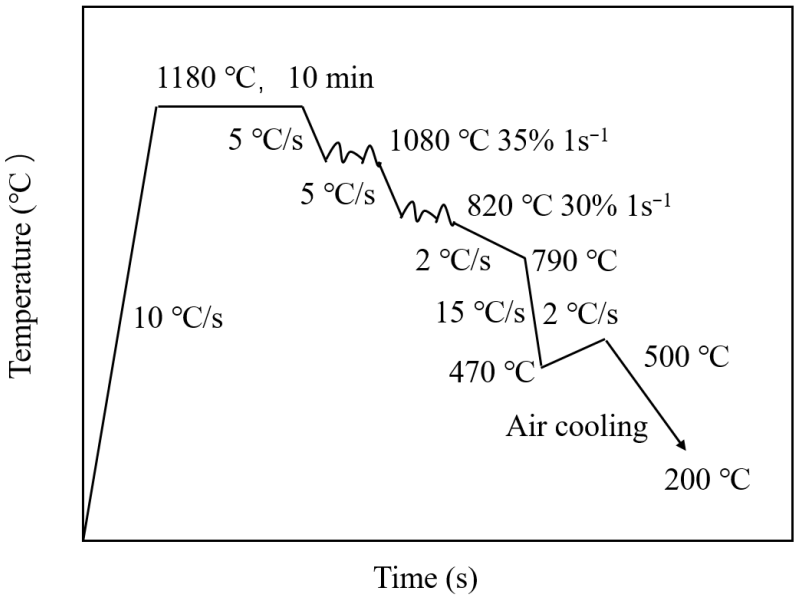


Figure 1. The TMCP used during the preparation of the test steel.

The materials were sectioned into 60 × 25 × 5 mm coupons. For metallographic preparation, all exposed faces were ground sequentially with 600#, 800#, and 1000-grit SiC paper to a uniform metallic finish. The coupons were then degreased in acetone, dried, and equilibrated in a desiccator for 24 h prior to analysis.

Table 1. Chemical compositions of test steels and reference steel.

Samples	C	Mn	Cu + Ni	Cr + V	Mo	Nb + V + Ti	Si	P	S	Als
0Mo	0.090	1.40	<1.0	<1.0	0	0.070	0.30	0.009	0.002	0.02
15Mo	0.088	1.42	<1.0	<1.0	0.15	0.071	0.29	0.008	0.003	0.02
30Mo	0.089	1.41	<1.0	<1.0	0.30	0.070	0.30	0.007	0.002	0.02
60Mo	0.088	1.42	<1.0	<1.0	0.60	0.069	0.29	0.008	0.002	0.02

2.2. Full-Immersion Corrosion Test

Full-immersion corrosion tests were conducted on the aforementioned experimental steels in accordance with the IMO Guidelines for the Inspection of Corrosion-Resistant Steel for Crude Oil Tanker Cargo Holds, aiming to investigate the effect of different Mo contents on the corrosion resistance of the steel [17]. The test temperature was maintained at 30 ± 1 °C, and the test solution was 10 wt.% NaCl. The test periods were set as 72, 120, 168, and 240 h, with three parallel specimens employed for each test condition. For rust removal and cleaning, the specimens were immersed in a descaling solution consisting of 500 mL of 36–38% HCl, 50 mL of deionized water, and 10 g of hexamethylenetetramine. After complete removal of corrosion products, the specimens were rinsed thoroughly with deionized water, followed by ultrasonic cleaning with anhydrous ethanol, and finally dried

and weighed. The annual average corrosion rate was calculated using Equation (1), with the results accurate to 0.1 mg [17]:

$$C.R. = \frac{365 \times 24 \times (G_0 - G) \times 10}{S \times T \times \rho} \quad (1)$$

where

C.R.—annual average corrosion rate, mm/a;
G—weight of the specimen after corrosion, g;
G_0—initial weight of the specimen before corrosion, g;
S—exposed surface area of the corroded specimen, cm^2;
ρ—density of the specimen, g/cm^3;
T—immersion corrosion test duration, h.

2.3. Characterization and Analysis of Corrosion Products

Microstructural examination of the corroded specimens was conducted using a Hitachi S-3400 scanning electron microscope (SEM) (Hitachi, Tokyo, Japan) at an accelerating voltage of 15 kV and a beam current of 40 mA. Phase analysis of the corrosion products was performed on a Rigaku D/max-2500/PC X-ray diffractometer (XRD) with Cu Kα radiation. Parameters were set at 40 kV and 200 mA, with a scan range of 10–75° (2θ) and a step size of 0.02°. Prior to analysis, consistent sample mass was maintained for comparative quantification. Data were processed using Jade 6.0 software, where phase ratios were calculated via the RIR method coupled with Rietveld refinement. X-ray photoelectron spectroscopy (XPS) analysis was carried out on a Thermo Scientific EscaLab 250xi system equipped with an Al Kα source. All spectra were calibrated by setting the adventitious carbon C 1s peak to 284.8 eV.

2.4. Electrochemical Measurements

The electrochemical behavior of the corroded specimens was assessed using a CHI660E workstation (Chenhua, Shanghai, China) in a standard three-electrode cell at room temperature. The electrolyte was a 10 wt.% NaCl solution, with the rusted specimen (1 cm^2 exposed) as the working electrode, a saturated calomel electrode (SCE) as the reference, and a platinum plate as the counter electrode. The system was stabilized by monitoring the open-circuit potential (OCP) for 1 h prior to testing. Potentiodynamic polarization was performed from −1.0 V to 0.1 V (vs. SCE) at a scan rate of 0.01667 mV/s. Electrochemical impedance spectroscopy (EIS) measurements were conducted over a frequency range of 10^5 to 10^{-2} Hz with a ±10 mV AC perturbation.

3. Results

3.1. Corrosion Kinetics

Figure 2 displays the corrosion kinetic curves for the four experimental steels with varying Mo contents under immersed conditions. The Mo-free steel shows the highest initial corrosion rate (~0.40 mm/a). With added Mo, the corrosion rate initially decreases to approximately 0.37 mm/a and 0.28 mm/a for the 15Mo and 30Mo steels, respectively, before rising again to about 0.33 mm/a for the 60Mo steel. When the corrosion period is extended to 240 h, the corrosion rates of all steels increase slightly, with the Mo-free reference steel still showing the maximum corrosion rate. This indicates that Mo addition can effectively inhibit the corrosion weight loss of the steel. Under the same corrosion period, 30Mo steel achieves the lowest corrosion rate, while excessive Mo content leads to a reverse increase in corrosion rate. These results demonstrate that an excessive amount of

Mo is not beneficial for enhancing the corrosion resistance of the steel. On the contrary, it impairs the corrosion resistance.

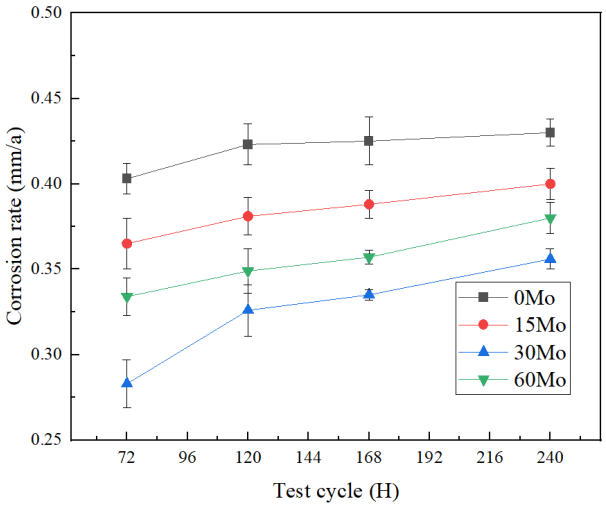


Figure 2. Corrosion kinetics of the four experimental steels under corrosive conditions.

3.2. Macroscopic Studies of Corrosion Products

Figure 3 compares the surface morphologies of the four steels after 120 h of corrosion. Their morphologies exhibit marked differences corresponding to Mo content. The Mo-free reference steel has large-sized and loosely distributed pores on its surface, which serve as the main channels for corrosive media to invade the matrix. An increase in Mo content correlates with a notable reduction in the number and size of pores within the surface corrosion product layer, indicating that Mo promotes densification. However, the 60Mo steel exhibits slightly more prominent surface porosity than the 30Mo steel, suggesting that excessive Mo may coincide with diminished microstructural homogeneity—highlighting a potential trade-off.

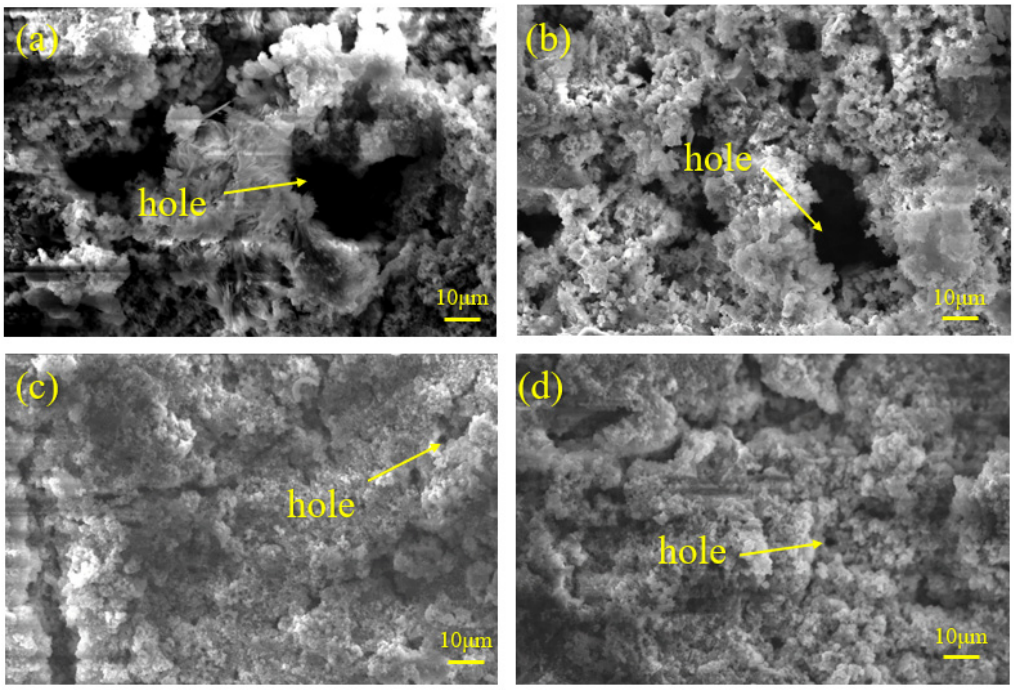


Figure 3. Surface morphologies of the four experimental steels after 120 h of corrosion test. (**a**) 0Mo; (**b**) 15Mo; (**c**) 30Mo; (**d**) 60Mo.

Figure 4 presents the surface morphologies of the four experimental steels after 240 h of the corrosion process. With the extension of the corrosion period, feather-like, worm-nest-like, and cotton-ball-like corrosion products can be observed. Yu et al. [18,19] reported that for weathering steel surfaces, feather-like and worm-nest-like substances are identified as γ-FeOOH and β-FeOOH with open structures, while clustered cotton-ball-like substances are regarded as relatively stable α-FeOOH. The Mo-free steel exhibits a mixed "feather-like + worm-nest-like" morphology with loose and irregular structures. For 15Mo steel, the number of pores in the corrosion products decreases, but local loose areas still persist. In addition, 30Mo steel shows a dense lamellar stacking structure of corrosion products, with refined and closely arranged particles and no obvious cracks, forming an effective physical barrier. The corrosion product structure of 60Mo steel is similar to that of 30Mo steel, but slight local agglomeration occurs, which may be attributed to the uneven precipitation of oxides induced by excessive Mo. This difference is associated with the formation mechanism of Mo oxides. During the corrosion process, the Mo generates nano-sized mixed oxides of MoO_2 and MoO_3 which can fill the pores of the rust layer, refine corrosion product particles, and enhance the compactness of the rust layer. Among all samples, the corrosion products of 30Mo steel are the most uniformly distributed with the optimal densification effect, which is consistent with the result that 30Mo steel exhibits the lowest corrosion rate in the corrosion kinetics analysis.

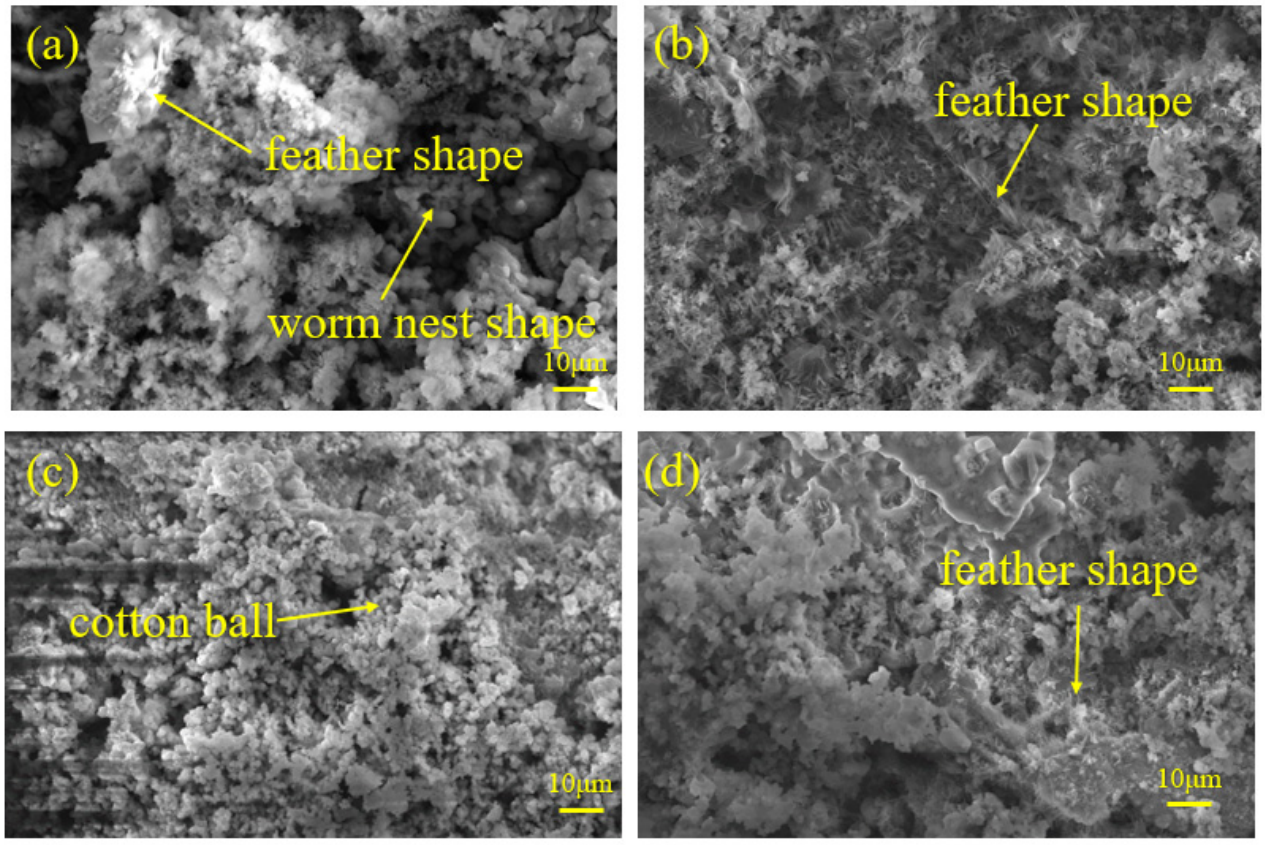


Figure 4. Surface morphologies of the four experimental steels after 240 h of corrosion test. (**a**) 0Mo; (**b**) 15Mo; (**c**) 30Mo; (**d**) 60Mo.

The cross-sectional morphologies of the rust layers on the four steels with different Mo contents after 240 h of exposure are presented in the SEM micrographs of Figure 5. As shown in Figure 5a, the Mo-free steel has a rust layer thickness of approximately 34 μm, featuring a loose structure and an uneven interface with the steel matrix with obvious gaps. These structural defects act as favorable channels for the infiltration of corrosive media,

endowing the rust layer with no protective capability. When the Mo content increases to 0.15 wt.%, the rust layer thickness of the steel reduces to 32 μm, with a slight improvement in structural compactness, yet local loose areas still remain. For 30Mo steel, the rust layer reaches a minimum thickness of only 20 μm, presenting a compact and uniform structure with a well-bonded interface to the steel matrix and no obvious defects. This structure can effectively block the invasion of corrosive media, thus serving as a robust physical barrier. However, when the Mo content further increases to 0.60 wt.%, the rust layer thickness of 60Mo steel rises to 28 μm, which is thicker than that of 30Mo steel. Meanwhile, the structural uniformity decreases, with pores and cracks emerging locally, leading to a decline in protective performance.

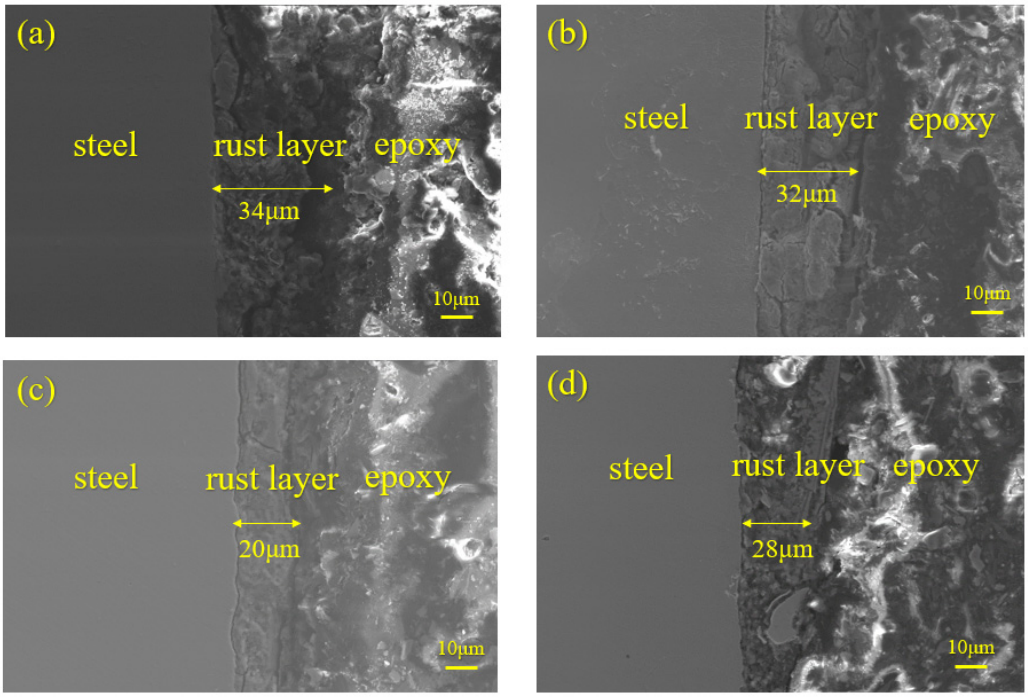


Figure 5. Cross-sectional SEM morphologies of the four experimental steels after 240 h of corrosion test. (**a**) 0Mo; (**b**) 15Mo; (**c**) 30Mo; (**d**) 60Mo.

The tests demonstrate that varying Mo contents significantly alter the rust layer's thickness and compactness. A moderate amount improves layer uniformity, whereas excessive Mo deteriorates its structure. Corrosion rate and morphology analyses corroborate this, indicating that 0.30 wt.% Mo provides the optimal equilibrium between protective performance and microstructural stability.

3.3. Composition of the Rust Layer

Figure 6 displays the XRD diffractograms of the experimental steels with varying Mo contents after 120 h and 240 h of corrosion. The corrosion products are constituted primarily by α-FeOOH, β-FeOOH, γ-FeOOH, Fe_3O_4, and amorphous material, with their relative proportions differing across the steel grades. As α-FeOOH is a stable, adherent phase that enhances passivation, the ratio of its content to the sum of the less stable phases (γ^* = β-FeOOH + γ-FeOOH + Fe_3O_4) is defined as a protective index (α/γ^*), where a higher value correlates with superior corrosion resistance [20,21].

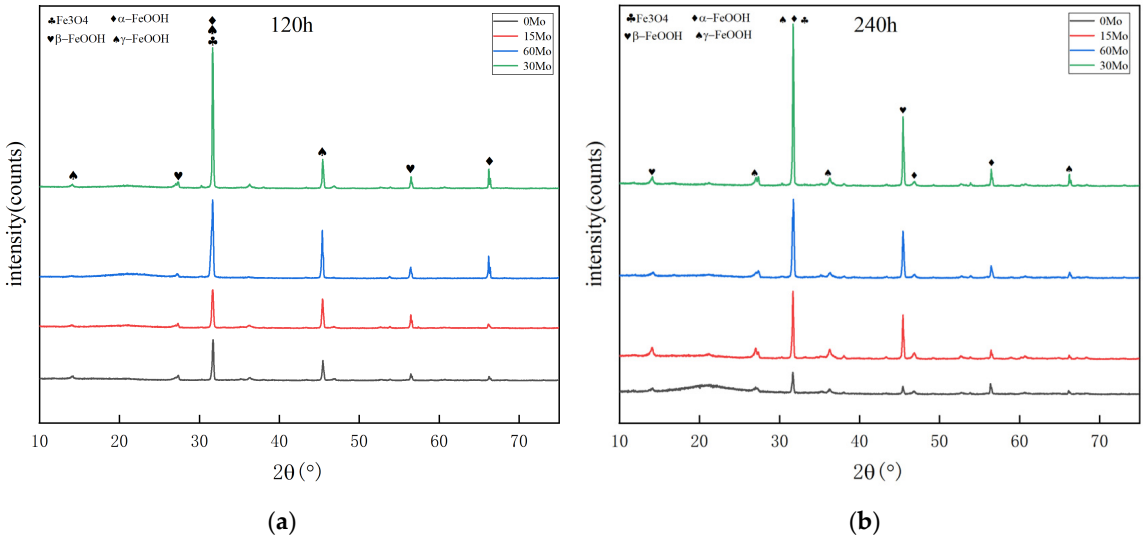


Figure 6. XRD patterns of the four experimental steels after different corrosion periods. (**a**) 120 h; (**b**) 240 h.

In order to further elucidate the role of Mo in shaping the phase structure of the corrosion products, a quantitative phase analysis based on the RIR method was conducted. The corresponding results are displayed in Figure 7. In terms of phase distribution, the Mo-free steel exhibits high relative contents of metastable phases (β-FeOOH and γ-FeOOH), while the Mo-containing steels have a higher relative content of the stable phase (α-FeOOH). This indicates that Mo can effectively promote the formation of stable phases. From the curve of the α/γ* ratio, the 30Mo specimen achieves the highest ratio of nearly 1.0 after 240 h of the corrosion process, whereas the ratios of the 0Mo, 15Mo and 60Mo specimens are all lower than that of the 30Mo specimen.

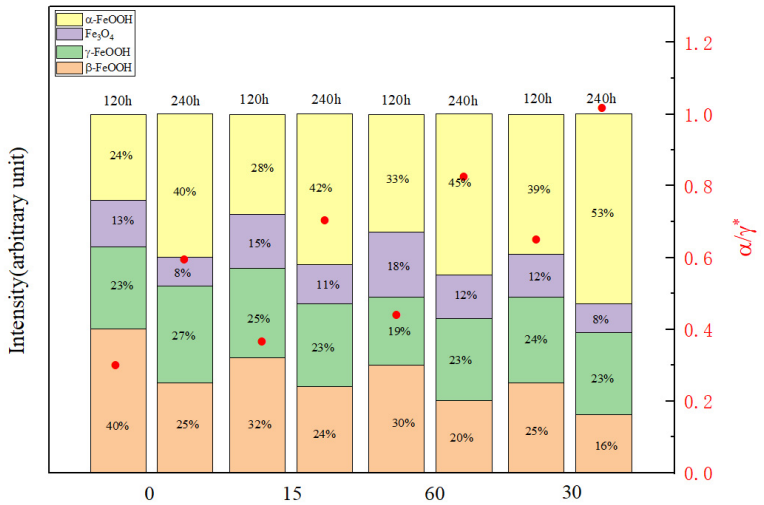


Figure 7. Phase structure distribution and α/γ* ratio plots of the four experimental steels in different corrosion periods.

These results demonstrate that Mo can facilitate the transformation of corrosion products from metastable phases to α-FeOOH, with the optimal transformation efficiency achieved at a Mo content of 0.30 wt.%, which maximizes the stability of the rust layer. The transformation effects of insufficient or excessive Mo are weaker than those of 0.30 wt.% Mo. This conclusion is consistent with the results of the corrosion rate and micromorphology analyses, further confirming that the 30Mo specimen possesses the optimal corrosion resistance.

Figure 8 illustrates the Mo $3d_3/_2$ XPS profiles for the corroded steels containing Mo. For the 15Mo steel, the spectrum is fitted with two peaks at 232.6 eV and 235.6 eV, assignable to MoO_2 and MoO_3, respectively [16]. Similarly, the Mo $3d_3/_2$ spectrum of the 30Mo specimen can also be split into two characteristic peaks, which share the same binding energies and corresponding substances as those of the 15Mo specimen. In contrast, the Mo $3d_3/_2$ spectrum of the 60Mo specimen is deconvoluted into three characteristic peaks, with binding energies of 226.1 eV, 231.9 eV, and 232.9 eV, corresponding to metallic Mo, MoO_2, and MoO_3, respectively [12]. A comparative analysis reveals that excessive Mo addition may lead to incomplete oxidation of Mo elements and the overgeneration of MoO_3, which tends to induce an increase in internal stress within the rust layer. This may account for the observed increase in corrosion rate with the further elevation of Mo content.

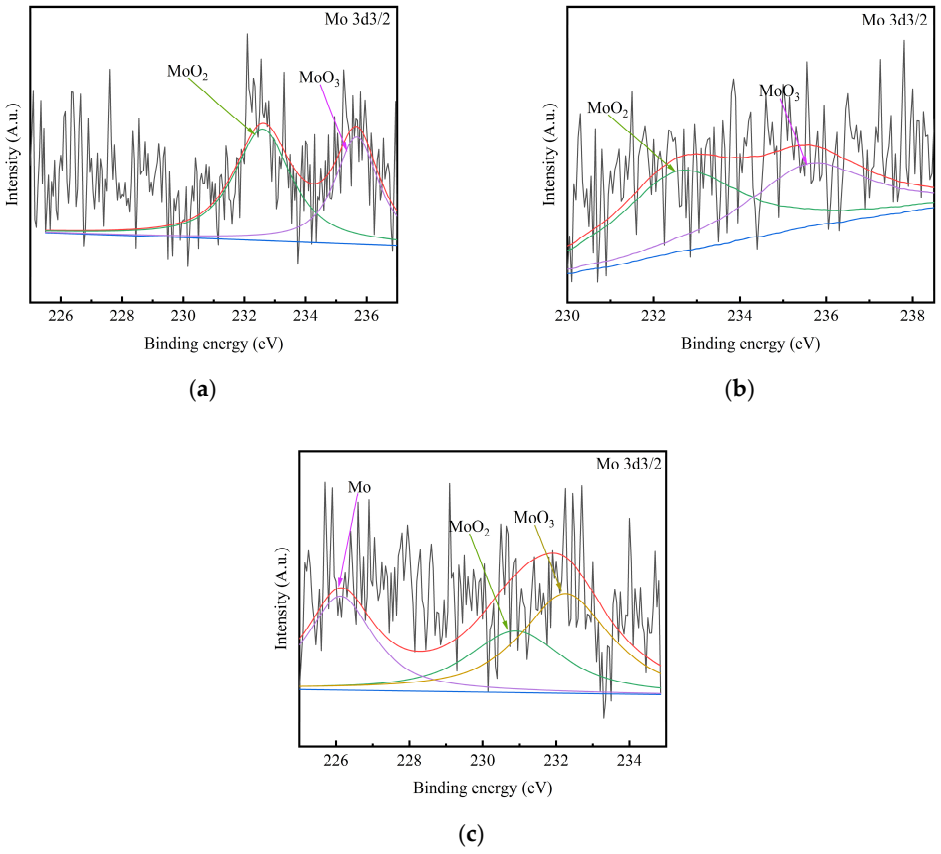


Figure 8. Mo $3d_3/_2$ XPS spectra of Mo-containing experimental steels after 240 h of corrosion. (**a**) 15Mo; (**b**) 30Mo; (**c**) 60Mo.

3.4. Electrochemical Properties of the Rust Layer

Figure 9 presents the Tafel polarization curves for the four experimental steels with varying Mo contents after immersion testing. The anodic branch is dominated by metal dissolution, while the cathodic branch is primarily attributed to the reduction of both corrosion products and dissolved oxygen [22,23]. Initially, after 120 h of the corrosion process, the Tafel curves of all specimens exhibit minor differences in the initial stage. However, with the extension of the corrosion period, distinct divergences emerge among the curves of different specimens. The Mo-free steel presents the most negative corrosion potential and a relatively high current density, indicating a strong corrosion tendency. The 30Mo specimen demonstrates a superior performance, characterized by a more positive potential and minimized current density. Furthermore, the evolution of the Tafel plots suggests that the influence of Mo content on electrochemical kinetics becomes increasingly evident with prolonged exposure. Hence, 0.30 wt.% Mo can effectively elevate the corrosion

potential and reduce the corrosion current density of the specimen, thereby attenuating its corrosion tendency.

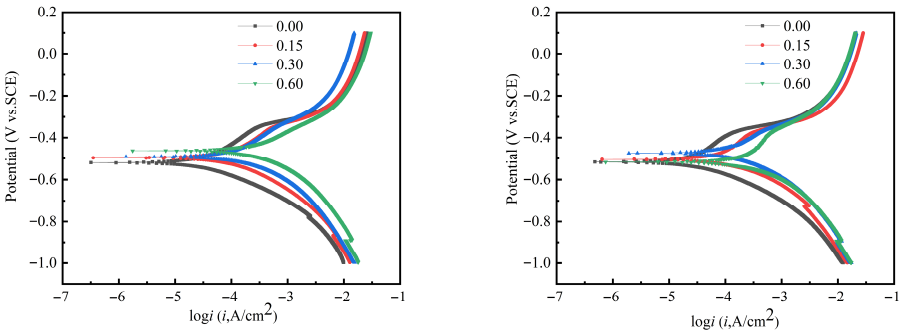


Figure 9. Tafel diagrams of the four test steels after full-immersion corrosion test. (**a**) 120 h; (**b**) 240 h.

For subsequent electrochemical analysis, the key parameters of corrosion potential (Ecorr) and corrosion current density (icorr) were determined for all four steels, utilizing the Tafel extrapolation method [24,25], with the results presented in Table 2.

Table 2 summarizes the Tafel curve parameters of the four experimental steels after 120 h and 240 h of corrosion. Generally speaking, a more positive Ecorr and a lower icorr indicate better corrosion resistance of the material. After 120 h of corrosion, the 0Mo specimen exhibited the most negative Ecorr and the highest icorr, suggesting the poorest corrosion resistance. In contrast, the 30Mo specimen showed the most positive Ecorr and the lowest icorr, demonstrating the optimal corrosion resistance. With the extension of the corrosion period, the Ecorr values of all specimens shifted positively, and the icorr values decreased slightly. Among them, the 30Mo specimen still maintained the most positive Ecorr and the lowest icorr after 240 h of corrosion. Mo addition enhanced the steel's electrochemical performance, as evidenced by the systematically nobler Ecorr and lower icorr of all doped specimens relative to the undoped reference. These findings confirm improved corrosion resistance. Notably, performance deterioration occurred with excessive Mo, indicating an optimal content range.

Table 2. Tafel curve parameters of the four test steels.

Samples	E_{corr}/V (vs. SCE)	I_{corr}/μA·cm^{-2}
120 h		
0	−0.520 ± 0.015	424.8 ± 3.4
15Mo	−0.511 ± 0.021	287.7 ± 2.4
30Mo	−0.501 ± 0.007	118.3 ± 7.2
60Mo	−0.509 ± 0.022	261.3 ± 1.6
240 h		
0	−0.517 ± 0.011	30.6 ± 2.1
15Mo	−0.505 ± 0.014	24.0 ± 3.7
30Mo	−0.445 ± 0.006	10.3 ± 1.9
60Mo	−0.487 ± 0.015	31.2 ± 2.1

The electrochemical impedance spectroscopy (EIS) spectra for the experimental steels with varying Mo contents are presented in Figure 10. The Bode magnitude plot reveals that the 30Mo specimen displays a superior capacitive response, maintaining the highest impedance modulus across the entire measured frequency range compared to the other steels. Especially in the low-frequency region, which corresponds to the penetration process of corrosive media, it achieves the maximum impedance modulus among all specimens,

indicating that the rust layer on the surface of the 30Mo specimen has stronger charge transfer resistance and corrosive medium penetration resistance [26]. In contrast, the 0Mo specimen maintains the lowest impedance modulus throughout the frequency range, reflecting the weakest barrier capability of its surface protective layer. The impedance modulus values of the 15Mo and 60Mo specimens fall between those of the 30Mo and 0Mo specimens, with the value of the 60Mo specimen being slightly lower than that of the 30Mo specimen. As observed from the phase angle curves, the 30Mo specimen presents a higher phase angle peak and a broader peak shape, demonstrating that its surface rust layer has a superior uniformity and compactness, along with greater polarization resistance against interfacial reactions [27].

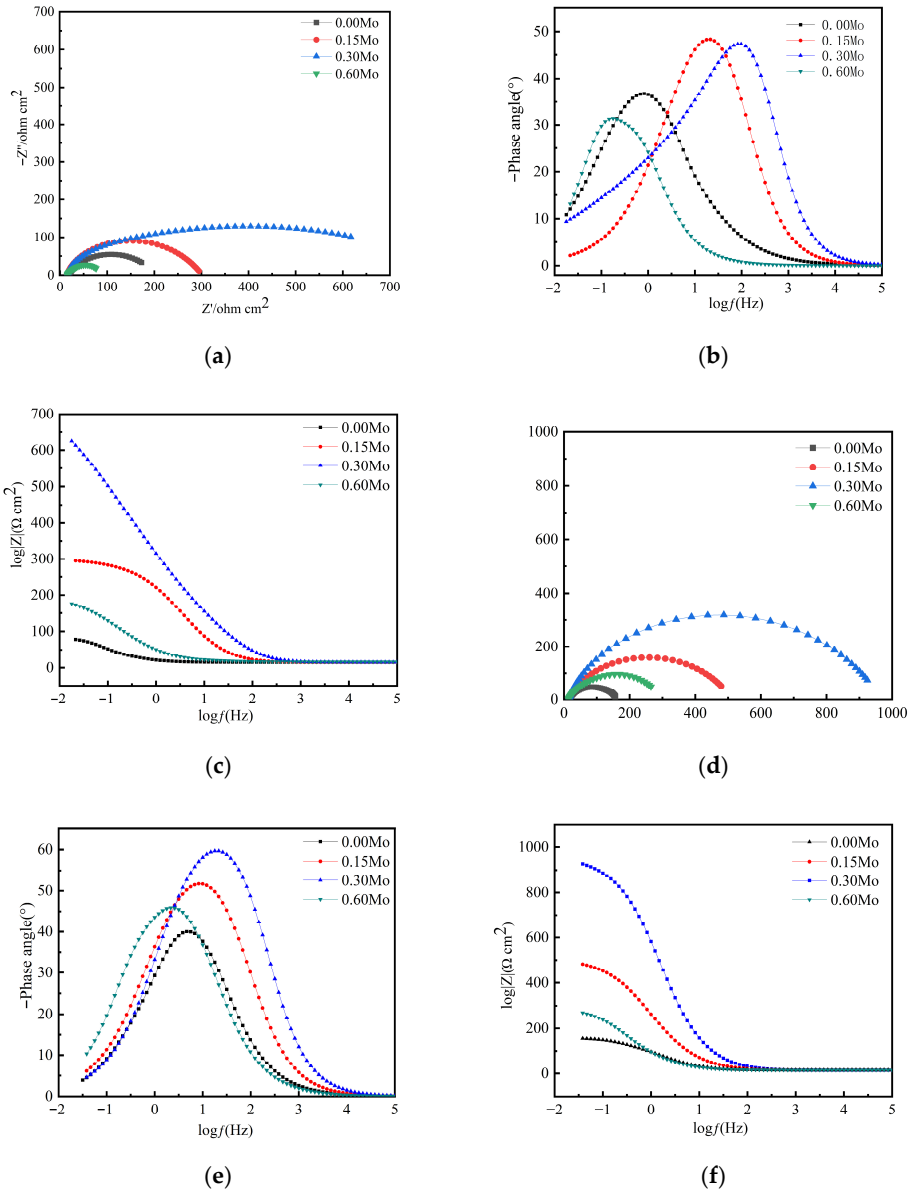


Figure 10. EIS spectra of the four experimental steels after full-immersion corrosion test. (**a**–**c**) 120 h; (**d**–**f**) 240 h; (**a**,**d**) Nyquist diagrams; (**b**,**c**,**e**,**f**) Bode diagrams.

A quantitative evaluation was performed by fitting the EIS curves with an equivalent circuit model in ZSimpin. In the Bode representation, the system exhibits a distinct phase maximum in the mid-frequencies, signifying a predominantly capacitive response. This behavior is consistent with an electrode process influenced by two time constants, namely those of the surface product layer and the electrochemical double layer. However, the

maximum phase angle is much lower than 90°, indicating that the electrode exhibits non-ideal capacitive characteristics due to porosity or relaxation effects. Thus, a constant phase element (Q) was employed to simulate this dispersion behavior during the EIS fitting process [28].

According to the existing literature [29,30], the experimental impedance data were well described by the equivalent circuit in Figure 11. In this model, the following notation is adopted: Rs denotes solution resistance; Rpore and Qf represent the resistance and constant phase element of the rust layer, respectively; and Rct and Qdl correspond to the charge-transfer resistance and double-layer constant phase element. The polarization resistance, Rp, is given by Rp = Rpore + Rct and is indicative of the overall corrosion resistance [31]. Figure 10 depicts the fitted polarization resistance (Rp) for each experimental condition.

As shown in the figure, the Rct value of the 0Mo specimen after 120 h of corrosion is only approximately 88.32 $\Omega \cdot cm^{-2}$, which increases to about 143.06 $\Omega \cdot cm^{-2}$ with the extension of the corrosion period, but remains the lowest among all specimens. Nevertheless, the addition of a certain amount of Mo to the steel leads to an increase in the Rct value. Specifically, the Rct value of the 30Mo specimen reaches 603 $\Omega \cdot cm^{-2}$ after 120 h of the corrosion process and rises to approximately 907.35 $\Omega \cdot cm^{-2}$ with a prolonged corrosion process, which is the highest among all specimens. These results indicate that the Rct value of all specimens increases with the extension of the corrosion period, suggesting that the rust layer is gradually formed and its protective effect is enhanced. Under the same corrosion period, the 30Mo specimen always exhibits a significantly higher Rct value than other specimens, indicating the largest interfacial charge transfer resistance, the most sluggish electrochemical corrosion process, and, thus, the optimal corrosion resistance. This experimental phenomenon is consistent with the results obtained from the aforementioned tests.

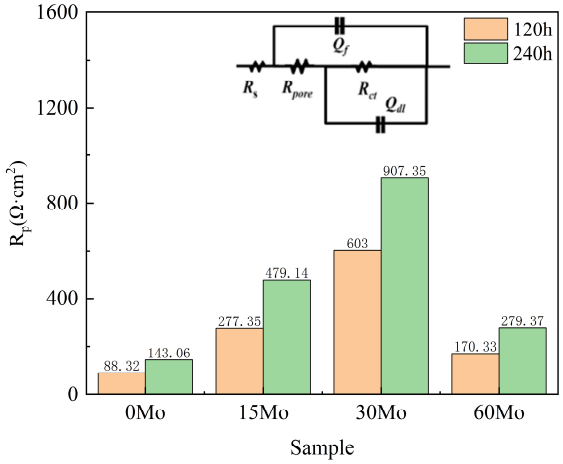


Figure 11. Rp values of the four experimental steels obtained from EIS fitting.

4. Discussion

Although widely used for storage tanks, low-alloy steels are susceptible to corrosion. Chloride ions constitute the predominant contributor to their in-service failure [32]. Generally, low-alloy steels undergo the following corrosion process during service: Fe is oxidized to Fe^{2+} via anodic dissolution, and the generated Fe^{2+} continuously hydrates to form a large amount of $Fe(O,OH)_6$. Then, the accumulation of these hydration products further generates FeOOH [33]. The corrosion products, identified in Figure 6 as α-, β-, and γ-FeOOH (with β- and γ- being dominant) [34], typically form a loose and porous layer. This permeable structure allows corrosive species to diffuse through to the substrate interface, initiating and accelerating localized corrosion at the steel surface. This explains

why the Mo-free experimental steel exhibits a relatively high corrosion rate, as shown in Figure 1.

When alloyed, Mo exhibits a standard electrode potential of −0.22 V, nobler than that of Fe (−0.44 V), Cr (−0.74 V), and Cu (−0.337 V) [15]. This implies that Mo is the least reactive in corrosive media, thus exhibiting lower electrochemical activity. Prolonged immersion leads to the progressive densification of the inner corrosion product layer. This microstructural evolution attenuates both mass transfer of dissolved oxygen and the kinetics of the oxygen reduction reaction. Subsequently, Mo gradually dissolves and undergoes the reactions shown in Equations (2)–(5). It can be seen that Mo is more likely to transform into stable MoO_2 and MoO_3 phases and simultaneously stabilize the surrounding unstable high-valence species, thereby optimizing the electrochemical stability of the interface. This is consistent with the observation that the electrochemical properties of the Mo-doped experimental steels are significantly improved, as presented in Figures 8 and 9 [11,15].

$$Mo + O_2 + 2H_2O \rightarrow Mo(OH)_4 \quad (2)$$

$$2Mo(OH)_4 + O_2 + 2H_2O \rightarrow 2Mo(OH)_6 \quad (3)$$

$$Mo(OH)_4 \rightarrow MoO_2 + 2H_2O \quad (4)$$

$$Mo(OH)_6 \rightarrow MoO_3 + 3H_2O \quad (5)$$

In the examined condition, Mo exists predominantly in the form of nanosized MoO_2 and MoO_3. These substances increase the nucleation sites of corrosion products and disrupt the initial 3D network structure of $Fe(OH)_3$, leading to the formation of finer corrosion products, thus achieving the refinement of corrosion product particles [21]. The comparative analysis in Figure 6 shows a substantially higher α-FeOOH content in Mo-bearing steels, demonstrating that Mo facilitates the stabilization of the rust layer by promoting the γ- to α-FeOOH transformation. This results in a more compact and adherent layer, consequently strengthening its barrier effectiveness and corrosion protection.

Meanwhile, it is observed that an excessively high Mo content leads to an increase in the corrosion rate. Combined with the results in Figure 7, metallic Mo is detected in the corrosion products of the steel with a high Mo content, whereas no metallic Mo is found in that with relatively low Mo contents. This indicates that excessive Mo tends to result in residual metallic Mo in the corrosion product layer or at the matrix interface due to incomplete oxidation. Given that the standard electrode potential of Mo (−0.22 V vs. SHE) is higher than that of Fe (−0.44 V vs. SHE), a galvanic cell system is formed when the two metals are in contact in the corrosive medium, with Fe acting as the anode and metallic Mo as the cathode. In this galvanic cell, anodic oxidation and dissolution reactions occur at the anode, while reduction reactions take place at the cathode [35]. The electrochemical reactions of the galvanic cell accelerate the dissolution of the Fe matrix at the anode, thereby exacerbating the corrosion of the experimental steels.

In addition, when the Mo addition amount is excessively high, the proportion of MoO_3 in the oxidation products increases significantly. From the perspective of the volume effect, the molar volume of MoO_2 is smaller than that of MoO_3 [15,36]. During the corrosion oxidation process, the massive formation of MoO_3 causes volume expansion inside the rust layer, which, in turn, generates significant internal stress. This internal stress disrupts the original dense structure of the rust layer and promotes the formation and propagation of microcracks and pores, as shown in Figures 3 and 4, directly leading to a decrease in the compactness of the rust layer. The deterioration of rust layer compactness weakens its physical barrier effect against corrosive media, making it easier for Cl^- to penetrate the rust layer and reach the steel matrix interface, thus accelerating the anodic dissolution

reaction. Together, the synergistic effect of this mechanism and the deterioration caused by the galvanic cell formed by residual metallic Mo due to excessive Mo addition result in the lower corrosion resistance of the high-Mo specimens compared with the 30Mo specimen. This further confirms that 0.30 wt.% is the optimal Mo addition content.

5. Conclusions

This work investigates the effect and underlying mechanism of Mo on the corrosion performance of tank steel in a simulated cargo oil tank environment. The research was conducted through a combination of long-term immersion tests, corrosion kinetics evaluation, detailed rust layer analysis, and electrochemical techniques. The key conclusions drawn are as follows:

1. Mo exerts a dual effect of enhancement at an appropriate dosage and deterioration at an excessive dosage on the corrosion resistance of tank steel, with 0.30 wt.% identified as the optimal addition content. At this dosage, the steel exhibits the lowest corrosion rate and optimal corrosion resistance; conversely, insufficient or excessive Mo addition leads to a significant reduction in protective efficacy.
2. An appropriate amount of Mo can optimize the structure and phase composition of the rust layer: it promotes the transformation of metastable γ-FeOOH to stable α-FeOOH, and the generated nanoscale Mo oxides fill the pores of the rust layer, rendering it compact and uniform. In contrast, excessive Mo results in an excessively high proportion of MoO_3, which induces increased internal stress within the rust layer, further causing rust layer thickening and the formation of structural defects.
3. The addition of 0.30 wt.% Mo optimally enhances the electrochemical stability of the steel, significantly elevating the corrosion potential while reducing the corrosion current density and charge transfer resistance. On the other hand, excessive Mo triggers the formation of Fe-Mo galvanic cells, which accelerate the corrosion reaction and consequently degrade the corrosion resistance of the steel.

Author Contributions: Conceptualization, J.H.; Methodology, J.H.; Software, Y.C.; Validation, Y.C. and C.Z.; Investigation, Y.Y. and Q.Y.; Resources, Y.Y., R.Z. and Q.Y.; Data curation, R.Z. and C.Z.; Writing—original draft, J.H.; Writing—review & editing, Q.W.; Project administration, Q.W.; Funding acquisition, Q.W. All authors have read and agreed to the published version of the manuscript.

Funding: The authors gratefully acknowledge the financial support from Cooperative Project of Nanjing Iron and Steel Co., Ltd.: Development and Application of High-Performance Corrosion-Resistant Crude Oil Storage Tanks Steel (IGAB20110006) and the Scientific Research and Innovation Project of Cangzhou Normal University (Grant No. cxtdl2301).

Data Availability Statement: The data presented in this study are available on request from the corresponding author. The data are not publicly available due to some of the data are still being used in other studies.

Conflicts of Interest: Author Jun Hong was employed by the Nanjing lron & Steel United Co., Ltd. The remaining authors declare that the research was conducted in the absence of any commercial or financial relationships that could be construed as a potential conflict of interest.

References

1. Hong, J.; Yang, Y.; Wang, Q. Effect of Mo on Microstructure and Mechanical Properties of Corrosion-Resistant Tank Steel. *Metals* **2025**, *15*, 926. [CrossRef]
2. Wei, J.-S.; Qi, Y.-C.; Tian, Z.-L.; Peng, Y. Corrosion Behavior of Welded Joints for Cargo Oil Tanks of Crude Oil Carrier. *J. Iron Steel Res. Int.* **2016**, *23*, 955–962. [CrossRef]
3. Wang, N.; Gao, J.; Xu, X. Effect of Mo on the Corrosion Resistance of Cr-Containing Steel in a Simulated Tropical Marine Atmospheric Environment. *Crystals* **2024**, *14*, 113. [CrossRef]

4. Ma, Y.; Li, Y.; Wang, F. Corrosion of low carbon steel in atmospheric environments of different chloride content. *Corros. Sci.* **2009**, *51*, 997–1006. [CrossRef]
5. Fan, Y.; Liu, W.; Sun, Z.; Chowwanonthapunya, T.; Zhao, Y.; Dong, B.; Zhang, T.; Banthukul, W. Effect of chloride ion on corrosion resistance of Ni-advanced weathering steel in simulated tropical marine atmosphere. *Constr. Build. Mater.* **2021**, *266*, 120937. [CrossRef]
6. Yu, Q.; Yang, X.; Dong, W.; Wang, Q.; Zhang, F.; Gu, X. Layer-by-layer investigation of the multilayer corrosion products for different Ni content weathering steel via a novel Pull-off testing. *Corros. Sci.* **2021**, *195*, 109988. [CrossRef]
7. Zhang, B.; Liu, W.; Sun, Y.; Yang, W.; Chen, L.; Xie, J.; Li, W. Corrosion behavior of the 3 wt.% Ni weathering steel with replacing 1 wt.% Cr in the simulated tropical marine atmospheric environment. *J. Phys. Chem. Solids* **2023**, *175*, 111221. [CrossRef]
8. Cano, H.; Díaz, I.; Fuente, D.D.L.; Chico, B.; Morcillo, M. Effect of Cu, Cr and Ni alloying elements on mechanical properties and atmospheric corrosion resistance of weathering steels in marine atmospheres of different aggressivities. *Mater. Corros.* **2018**, *69*, 18–19. [CrossRef]
9. Cano, H.; Neff, D.; Morcillo, M.; Dillmann, P.; Diaz, I.; de La Fuente, D. Characterization of corrosion products formed on Ni 2.4 wt%-Cu 0.5 wt%-Cr 0.5 wt% weathering steel exposed in marine atmospheres. *Corros. Sci.* **2014**, *87*, 438–451. [CrossRef]
10. Sun, Y.; Liu, W.; Sun, Z.; Li, H.; Zhang, B.; Yang, W.; Chen, L.; Dong, B.; Zhang, T. Optimizing microstructure for enhanced atmospheric corrosion resistance of a novel Ni–Mo weathering steel: A field exposure study in Thailand's tropical marine environment. *Vacuum* **2024**, *221*, 112876. [CrossRef]
11. Jamadar, A.S.; Pedanekar, R.S.; Lee, S.C.; Kim, S.J. Electrochemical and compositional insights into early-stage corrosion behavior of High-Mn steel microalloyed with Cr, Mo, and V in 3.5% NaCl solution. *Electrochim. Acta* **2025**, *536*, 146744. [CrossRef]
12. Xu, X.; Zhang, T.; Wu, W.; Jiang, S.; Yang, J.; Liu, Z. Optimizing the resistance of Ni-advanced weathering steel to marine atmospheric corrosion with the addition of Al or Mo. *Constr. Build. Mater.* **2021**, *279*, 122341. [CrossRef]
13. Sun, Y.; Liu, W.; Dong, B.; Zhang, T.; Chen, L.; Yang, W.; Li, H.; Zhang, B.; Xie, J.; Cui, J. Designing weathering steel with optimized Mo/Ni ratios for better corrosion resistance in simulated tropical marine atmosphere. *Met. Mater. Int.* **2024**, *30*, 909–927. [CrossRef]
14. Han, C.; Yu, Q.; Wang, S.; Qiao, M.; Wang, Q. Research on the Influence of Mo on the Corrosion Mechanism of 1%Ni Weathering Steel in Simulated Marine Atmospheric Environments. *Metals* **2025**, *15*, 430. [CrossRef]
15. Sun, M.; Pang, Y.; Du, C.; Li, X.; Wu, Y. Optimization of Mo on the corrosion resistance of Cr-advanced weathering steel designed for tropical marine atmosphere. *Constr. Build. Mater.* **2021**, *302*, 124346. [CrossRef]
16. Zhang, T.; Liu, W.; Chen, L.; Dong, B.; Yang, W.; Fan, Y.; Zhao, Y. On how the corrosion behavior and the functions of Cu, Ni and Mo of the weathering steel in environments with different NaCl concentrations. *Corros. Sci.* **2021**, *192*, 109851. [CrossRef]
17. *MSC 289 (87)*; Sets Standards for Ships. Ports & Harbors Resolut. IMO: London, UK, 2010.
18. Yu, Q.; Dong, W.; Yang, X.; Wang, Q.; Zhang, F. Insights into the corrosion mechanism and electrochemical properties of the rust layer evolution for weathering steel with various Cl deposition in the simulated atmosphere. *Mater. Res. Express* **2021**, *8*, 36515–36518. [CrossRef]
19. Yu, Q.; Dong, W.; Yang, X.; Wang, Q.; Zhang, F. The Role of the Direct Current Electric Field in Enhancing the Protective Rust Layer of Weathering Steel. *J. Mater. Eng. Perform.* **2021**, *30*, 6309–6322. [CrossRef]
20. Kamimura, T.; Hara, S.; Miyuki, H.; Yamashita, M.; Uchida, H. Composition and protective ability of rust layer formed on weathering steel exposed to various environments. *Corros. Sci.* **2006**, *48*, 2799–2812. [CrossRef]
21. Kimura, M.; Kihira, H.; Ohta, N.; Hashimoto, M.; Senuma, T. Control of $Fe(O,OH)_6$ nano-network structures of rust for high atmospheric-corrosion resistance. *Corros. Sci.* **2005**, *47*, 2499–2509. [CrossRef]
22. Hao, L.; Zhang, S.; Dong, J.; Ke, W. Evolution of corrosion of MnCuP weathering steel submitted to wet/dry cyclic tests in a simulated coastal atmosphere. *Corros. Sci.* **2012**, *58*, 175–180. [CrossRef]
23. Chen, Z.; Yu, Q.; Zhao, L.; Zhang, C.; Gu, M.; Wang, Q.; Wang, G. Insight into the role of Si on corrosion resistance of weathering steel in a simulated industrial atmosphere. *J. Mater. Res. Technol.* **2023**, *26*, 487–503. [CrossRef]
24. Mccafferty, E. Validation of corrosion rates measured by the Tafel extrapolation method. *Corros. Sci.* **2005**, *47*, 3202–3215. [CrossRef]
25. Mansfeld, F. Tafel slopes and corrosion rates obtained in the pre-Tafel region of polarization curves. *Corros. Sci.* **2005**, *47*, 3178–3186. [CrossRef]
26. Collazo, A.; Nóvoa, X.R.; Pérez, C.; Puga, B. EIS study of the rust converter effectiveness under different conditions. *Electrochim. Acta* **2008**, *53*, 7565–7574. [CrossRef]
27. Thee, C.; Hao, L.; Dong, J.H.; Mu, X.; Ke, W. Numerical Approach for Atmospheric Corrosion Monitoring Based on EIS of a Weathering Steel. *Acta Metall. Sin.* **2015**, *11*, 261–271. [CrossRef]
28. Li, Y.; Xu, J. Is niobium more corrosion-resistant than commercially pure titanium in fluoride-containing artificial saliva? *Electrochim. Acta* **2017**, *233*, 151–166. [CrossRef]

29. Nishikata, A.; Ichihara, Y.; Tsuru, T. An application of electrochemical impedance spectroscopy to atmospheric corrosion study. *Corros. Sci.* **1995**, *37*, 897–911. [CrossRef]
30. Barcia, O.E.; D'Elia, E.; Frateur, I.; Mattos, O.R.; Tribollet, B. Application of the impedance model of de Levie for the characterization of porous electrodes. *Electrochim. Acta* **2002**, *47*, 2109–2116. [CrossRef]
31. Yu, Q.; Li, B.; Wang, F.; Tai, J.; Liu, P. The role of stabilization technology on the enhancement of corrosion resistance and corrosion mechanism for weathering steel. *Mater. Today Commun.* **2024**, *40*, 109694. [CrossRef]
32. Zhang, X.; Yang, S.; Zhang, W.; Guo, H.; He, X. Influence of outer rust layers on corrosion of carbon steel and weathering steel during wet–dry cycles. *Corros. Sci.* **2014**, *82*, 165–172. [CrossRef]
33. Morcillo, M.; Chico, B.; Diaz, I.; Cano, H.; Fuente, D.D.L. Atmospheric corrosion data of weathering steels. A review. *Corros. Sci.* **2013**, *77*, 6–24. [CrossRef]
34. Jia, J.; Liu, Z.; Cheng, X.; Du, C.; Li, X. Development and optimization of Ni-advanced weathering steel: A review. *Corros. Commun.* **2021**, *2*, 82–90. [CrossRef]
35. Chiavari, C.; Bernardi, E.; Martini, C.; Passarini, F.; Motori, A.; Bignozzi, M.C. Atmospheric corrosion of Cor-Ten steel with different surface finish: Accelerated ageing and metal release. *Mater. Chem. Phys.* **2012**, *136*, 477–486. [CrossRef]
36. Sun, M.; Xiao, X.; Xu, X.; Li, J.; Zhao, T.; Gong, L.; Du, C.; Li, X. Effect of Mo and Sn co-regulation on low alloy steel corrosion in tropical marine atmosphere. *NPJ Mat. Degrad.* **2024**, *8*, 92. [CrossRef]

Disclaimer/Publisher's Note: The statements, opinions and data contained in all publications are solely those of the individual author(s) and contributor(s) and not of MDPI and/or the editor(s). MDPI and/or the editor(s) disclaim responsibility for any injury to people or property resulting from any ideas, methods, instructions or products referred to in the content.